Evidence for strain induced conductance modulations in single-layered graphene on SO_2

Andrew P. Lai
Mentor: Nai-Chang Yeh
Co-mentor: Marcus Teague

May 5, 2009

Contents

1 Abstract

The unique physical properties of graphene and its potential uses in nanoscale devices make it a compelling subject of study.[1] Graphene, a two dimensional crystal which consists of a single layer of carbon atoms bonded together in a hexagonal lattice, has a conical band structure at low energies. Therefore, the charge carriers of graphene obey the Dirac equation for relativistic particles and can be thought of as massless Dirac fermions.[1,2,3] However, recent scanning tunneling microscopy (STM) studies of graphene on silicon dioxide substrates have found corrugations in the graphene samples, and more importantly have observed deviations in the tunneling spectra from the expected Dirac-like behavior.[4,5,6] Several possible explanations exists for this observed deviation from Dirac-like behavior, including phonon-mediated inelastic tunneling [4,7], charge impurities [6], and changes to the band structure to due the underlying substrate.[8]

We present scanning tunneling spectroscopy and microscopy data of graphene on a silicon dioxide substrate at a temperature of 77 K. The topographical studies reveal surface corrugations in graphene due to rippling and partial conformation to the underlying silicon dioxide substrate. In the tunneling spectra, a deviation from the expected Dirac-like behavior is observed. A lack of correlation between the Dirac voltage and conductance maps at a low bias voltage indicates charge impurities are not the primary cause for deviations from Dirac-like behavior. A strain map is computed from the topography and green's functions are fitted to estimate the contribution of phonon coupling to the tunneling conductance. We find that regions of higher strain correspond to higher phonon frequencies, indicating that phonon-mediated inelastic tunneling is a major contributor to the deviation from Dirac-like behavior found in tunneling spectra.

2 Introduction/Background

Prior to its successful isolation, graphene was believed not to exist naturally in nature due to arguments made by Landau and Peierls that 2D crystals were thermodynamically unstable.[9,10] Graphene was only recently mechanically isolated in 2004 by A.K. Geim

and K.S Novoselov from the University of Manchester. [1] In the short time since it was successfully isolated, many remarkable properties have been found in graphene, such as Dirac-like band structure; an ambipolar electric field effect, which allows the charge carriers to be tuned continuously from electron to holes[1]; exceptionally high mobilities of up to $200000 cm^2 V^{-1} s^{-1}$ at ambient conditions[11,12]; and a minimum conductance of $\frac{4e^2}{h}$ when gated at zero charge carriers[13,14], where e is the charge of an electron and h is Planck's constant.

2.1 Fabrication of Graphene

The first graphene flakes observed were produced through the process of mechanical exfoliation.[1] Mechanically exfoliation involves repeatedly peeling graphite with scotch tape, until flakes of few layer or single layer graphene are achieved. In order to investigate whether these flakes are truly single layered graphene, the flakes are placed on top of a silicon dioxide substrate of precisely 300 nm thickness. Due to optical interference, single layered graphene can then be identifed with an optical microscope.

While mechanical exfoliation is a relatively inexpensive process for fabricating graphene, it is a time consuming and yields graphene flakes of sizes only on the order of several microns in size. A lot of effort has therefore been placed in attempting to grow graphene epitaxially. Single layer graphene has successfully been grown through chemical vapour deposition of hydrocarbons on metallic surfaces, as well as through thermodeposition on silicon carbide. As of recently, graphene samples of areas up to several square centimeters have been grown using chemical vapour deposition of nanometer thick graphite films onto a nickel substrate.[15]

2.2 Electronic Band structure of Graphene

Graphene exhibits a unique electronic band structure which is conical and has no band gap at the K and K′ points of the Brillioun zone. Each carbon atom in graphene has four valence electrons; the three σ electrons are covalently bonded to neighboring carbon atoms through sp^2 hybridization while the remaining π electron is in the $2p_z$ orbital

and participates in conduction through the graphene sheet.[16] Consequently, we are only interested in the $2p_z$ electrons and we will use a tight binding approximation to calculate the electronic band structure of graphene [16,17]

2.2.1 Tight Binding Approximation

Let us now consider the bravais lattice of graphene. The unit cell consists of 2 atoms; typically denoted as A atoms and B atoms. A general electronic wavefunction $\Psi(\vec{r})$ will be sought of the form:

$$\Psi(\vec{r}) = c_A\Phi_A(\vec{r}) + c_B\Phi_B(\vec{r} - \vec{d}) \qquad (1)$$

where Φ_A and Φ_B have the form satisfying Bloch's Theorem

$$\Phi_\alpha(\vec{r}) = \frac{1}{\sqrt{N}}\sum_{\vec{R}} e^{i\vec{k}\cdot\vec{R}}\psi_\alpha(\vec{r} - \vec{R}),\ \alpha = A, B \qquad (2)$$

and ψ_A and ψ_B are the $2p_z$ wavefunctions at lattice sites A and B.

To find the electronic band structure of graphene, the secular equation [17]

$$\det(H - ES) = 0 \qquad (3)$$

will be solved for energy, where H is the Hamiltonian, E is the eigenenergy and S is the overlap integral matrix. The matrix elements of H and S will be computed considering only the three nearest neighbors of each atom. The notation where H_{AB} is the matrix element $< \Phi_A|H|\Phi_B >$ will be used.

Since the three nearest neighbors of each A atom are three B atoms and vice versa, H_{AA} and H_{BB} are 0. For H_{AB} and H_{BA}, there 3 B atoms surrounding the A atoms and vice versa. Therefore:

$$H_{AB} = H_{BA} = \sum_k e^{i\vec{k}\cdot\vec{R}_k}t_k,\ \mathrm{k} = 1,\ 2,\ 3 \qquad (4)$$

$$t_k =< \psi_A(\vec{r})|H|\psi_B(\vec{r} - \vec{R}_k) >$$

where $\vec{k}$ is the wavenumber and $t = t_1 = t_2 = t_3$. For convenience, we denote

$f_A(k) = \sum_k e^{i\vec{k}\cdot\vec{R}_k} t$. Now, the distances from atom A to its three B neighbors are (for a B atom to its nearest A neighbors, $R_{ib} = -R_{ia}$):

$R_1 = (\frac{a}{2\sqrt{3}}, \frac{a}{2})$

$R_2 = (\frac{a}{2\sqrt{3}}, -\frac{a}{2})$

$R_3 = (-\frac{a}{\sqrt{3}}, 0)$

where a = 2.49 $\mathring{A}$. Therefore $f_A(k) = t(e^{ik_x \frac{a}{\sqrt{3}}} + 2e^{-ik_x \frac{a}{2\sqrt{3}}} \cos\frac{k_y a}{2})$. Note that $f(k)_B = f_A(k)^* = f(k)$. Therefore, $H_{AB} = H^*_{BA} = f(k)$

In calculating the overlap integral matrix, for $s_k =< \psi_A(\vec{r})|\psi_B(\vec{r} - \vec{R_k}) >$, we have assumed that $s_k << 1$ in the tight binding approximation, so that $S_{AA} = S_{BB} = 1$ and $S_{AB} = S_{BA} = 0$.

Setting $E_{2p_z} = 0 \Rightarrow$

$$\det \begin{bmatrix} -E & f(k) \\ f(k)^* & 2-E \end{bmatrix} = 0 \Rightarrow$$

$E^2 = |f(k)|^2 \Rightarrow$

$$E_{2D}(k_x, k_y) = \pm t\sqrt{1 + 4\cos\frac{\sqrt{3}k_x a}{2}\cos\frac{k_y a}{2} + 4\cos^2\frac{k_y a}{2}} \qquad (5)$$

where $t \approx$ -3.033 eV. These two bands meet at the six corners known as the K and K′ points of the first Brillouin zone of the reciprocal lattice, and therefore graphene has no band gap (Figure 1).

2.2.2 Relativistic Charge Carriers

Taylor expanding E_{2D} near the K or K′ points in the first Brillouin zone to first order gives:

$$E_{2D}(k_x, k_y) \approx \pm v_f \hbar|\vec{k}| \qquad (1)$$

where v_f is the Fermi velocity with a value of $\approx \frac{c}{300}$. As a result of this conical band structure, charge carriers of graphene at energies near E_d have vanishing effective mass

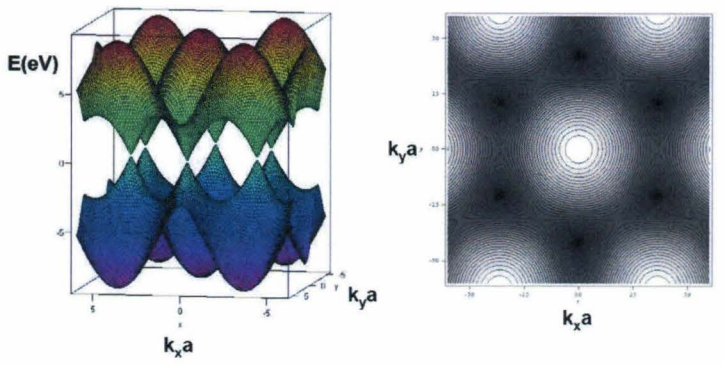

Figure 1: The band structure of graphene (images taken from Heo, Jinseong. Probing electronic properties of carbon nanotubes. Ph.D thesis. California Institute of Technology). (2008)

and obey the Dirac equation for relativistic particles, with a reduced speed of light equal to v_f. Therefore, these charge carriers can be thought of as massless Dirac fermions.

2.3 Electronic Transport in Graphene

Experimental studies [1,11,12] have shown a remarkably high charge carrier mobility μ in graphene. Specifically, mobilities of up to $200000\frac{cm^2}{Vs}$ at ambient conditions have been measured, which are larger than the highest mobilities of any semiconducting materials. This measured value is in agreement with the predicted value assuming charge impurities in the substrate as the main source of scattering. The high mobilities make graphene an excellent candidate to be be used in components of integrated circuits and it is highly possible that graphene will replace current silicon based technologies.

The high charge carrier mobilities of graphene also allow for the observation of the Quantum Hall Effect (QHE) at room temperature.[18] Graphene exhibits an anamolous QHE, where the hall conductance plateau occur at $\sigma_{xy} = \pm(N + \frac{1}{2})\frac{4e^2}{h}$, which compared to the standard Integer Quantum Hall effect sequence is shifted by $\frac{1}{2}$. Additionally, due to the relativistic nature of the charge carriers of graphene, the energies of the Landau Levels in a magnetic field are given by are $E_N = \pm v_f\sqrt{2e\hbar BN}$, instead of the standard $E_n = E_\pm \pm \hbar\omega_c(n + \frac{1}{2})$, where $\omega_c = \frac{eB}{m*}$ is the cyclotron frequency.

Graphene also exhibits an ambipolar electric field effect[1], where the concentration of charge carriers can be tuned continously from electrons to holes by adjusting the gate

voltage.

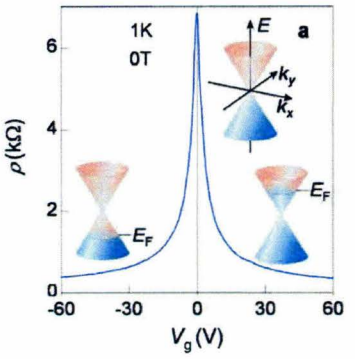

Figure 2: The ambipolar electric field effect in graphene. Changing the gate voltage in graphene changes the fermi level, allowing for the concentration of charge carriers to be tuned continously from electron to holes. The rapid decrease in resistivity when increasing the charge carrier concentation indicates their high mobility. (Image taken from Rise of graphene. K.S Novoselov, et. al. 2007)

When the density of charge carriers is gated to zero, graphene still exhibits a finite conductivity of $\frac{4e^2}{h}$.[13,14] This minimum conductively is a property instrinsic to systems described by the Dirac equation [11]. Most theories perdict a value of $\frac{4e^2}{\pi h}$ for the minimum conductivity of graphene, in constrast to the $\frac{4e^2}{h}$ found in most experimental measurements. It is not yet known whether this disagreement is due to theoretical approximations of electron scattering in graphene, or experimental limitations in measurements.

2.4 Scanning Tunneling Microscopy

An excellent tool for investigating graphitic surfaces is the scanning tunneling microscope (STM).[19,20] Scanning tunneling microscopy operates on the principle of quantum tunneling, where a small voltage is applied between a conducting tip and sample, establishing a tunneling current between the two. The tunneling current is proportional exponentially to the distance between the STM tip and the sample, and therefore can provide information about the topography of the sample with rather high precision. The derivative of the tunneling current with respect to bias voltage is proportional to the local density of states (LDOS) of the sample, and therefore the STM can provide spatial resolution of the LDOS of a sample.

3 Deviation from Dirac-like behavior

Recent studies on graphene have produced observed spectra which does not exhibit Dirac-like behavior.[5,6,8] There are several interpretations for the cause of this deviation from Dirac behavior. Charge impurties will cause a shift in the Dirac point, and therefore cause a deviation in observations from the expected behavior.[6] Phonon-mediated inelastic tunneling[1]1 will also have an affect on the tunneling spectra, due to coupling between the nearly free electron bands at the center of the Brillouin zone and the π bands at K and K′.[5,7] Finally, studies of graphene on silicon carbide have found that some of the π bonds typically involved in conduction have instead bonded with carbon atoms in the substrate, therefore changing the electronic band structure of graphene and giving rise to finite energy gaps[8].

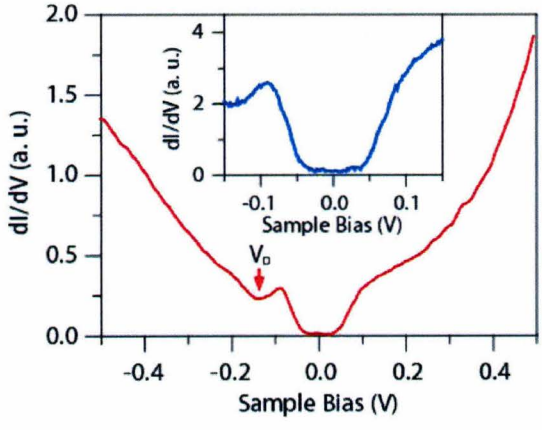

Figure 3: The tunneling spectra over corrugated graphene. The deviation from Dirac-like behavior is attributed to phonon-mediated inelastic tunneling. (Image taken from Giant Phonon-induced Conductance in Scanning Tunneling Spectroscopy of Gate-tunable Graphene. Y. Zhang, et al. (2008)

As a simple excercise, we will first consider a uniaxial strain on a graphene lattice. This serves as a very rough approximation of the distortion to the topological structure caused by the corrugations.

3.1 Electronic Band Structure of strained graphene

The deviation from Dirac-like behavior has been observed mostly in corrugated graphene samples. Therefore, as a simple approximation, the corrugations on the graphene samples will be approximated as a strain in the graphene lattice to see if such a disortion would cause graphene to lose its conical band structure and induce a band gap.

3.1.1 Uniaxial strain

The tight binding calculation used to derive the band structure of graphene will be redone considering the effects of the strain σ in the direction depicted in Figure 4.

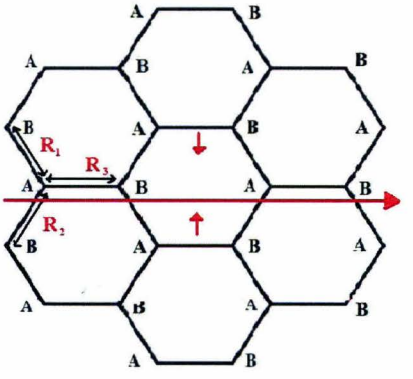

Figure 4: Strain along the horizontal direction. Note that there is a compression in the direction transverse to the strain

There will also be a contraction in the direction transverse to the strain, which will be depedent on ν, the poisson ratio of graphene.[16] It will be assumed that the strain is not sufficient to invalidate the three nearest neighbors approximation, so H_{AA} and H_{BB} will still be zero and only H_{AB} and H_{BA} will need to be recomputed. The distances of the A atom to its three nearest B neighbors are:

$$R_1 = (\frac{(1+\sigma)a}{2\sqrt{3}}, \frac{(1-\nu\sigma)a}{2})$$
$$R_2 = (\frac{(1+\sigma)a}{2\sqrt{3}}, -\frac{(1-\nu\sigma)a}{2})$$
$$R_3 = (-\frac{(1+\sigma)\gamma a}{\sqrt{3}}, 0)$$

$$H_{AB} = H_{BA} = \sum_k e^{i\vec{k}\cdot\vec{R}_k} t_k, \text{ k = 1, 2, 3}$$

$$t_k = < \psi_A(\vec{r})|H|\psi_B(\vec{r} - \vec{R}_k) >$$

By symmetry, $t_1 = t_2 = t$. Let $t_3 = c_t t$ and $f(k) = \sum_k e^{i\vec{k}\cdot\vec{R}_k} t_k$. This means that $f(k)_A = t(c_t e^{i(1+\sigma)k_x \frac{a}{\sqrt{3}}} + 2e^{-i(1+\sigma)k_x \frac{a}{2\sqrt{3}}} \cos\frac{(1-\nu\sigma)k_y a}{2})$. Note that $f(k)_A = f(k)_B{}^* = f(k)$. Therefore, $H_{AB} = H^*_{BA} = f(k)$

Reformulating the earlier calculation:

$$E_{2D}(k_x, k_y) = \pm t\sqrt{{c_t}^2 + 4c_t \cos\frac{\sqrt{3}(1+\sigma)k_x a}{2} \cos\frac{(1-\nu\sigma)k_y a}{2} + 4\cos^2\frac{(1-\nu\sigma)k_y a}{2}} \qquad (1)$$

3.1.2 Low Energy dispersion

Taylor expanding E^2_{2D} near a minima at low energies and keeping only the lowest terms...

$$E^2_{2D} \approx \tfrac{3}{4}c_t(1+\sigma)^2(ak'_x)^2 + (1-\tfrac{c_t^2}{4})(1-\nu\sigma)^2(ak'_y)^2 \Rightarrow$$

$$E_{2D}(k'_x, k'_y) \approx \pm ta\sqrt{\tfrac{3}{4}c_t(1+\sigma)^2{k'_x}^2 + (1-\tfrac{c_t^2}{4})(1-\nu\sigma)^2{k'_y}^2}$$

Therefore, the dispersion relation is still conical, and the band gap is still exactly zero.

3.1.3 Strain along any axis

Up to this point, we have restricted our consideration to uniaxial strain parallel to one of the sides of the hexagon. Next, we relax the constraint and allow strain σ along an arbitrary axis, $\hat{c} = \cos\theta\hat{x} + \sin\theta\hat{y}$. Due to the strain, there will be a compression (or stretch, if the strain is a compression) in the axis perpendicular to that of $\hat{c}$, which we denote as $\hat{n} = \sin\theta\hat{x} - \cos\theta\hat{y}$. This compression will be dependent on the poisson ratio ν of graphene, which is about 0.17. [16] Remaining with the three nearest neighbors approximation, for each A atom (for B atoms, simply negate the R_i components):

$$\vec{R_i}' = \vec{R_i} + \sigma((\vec{R_i}\cdot\hat{c})\hat{c} - \nu(\vec{R_i}\cdot\hat{n})\hat{n})$$

so we now have (assuming units where a = 1):

$$R_{1x} = (\tfrac{1}{2\sqrt{3}} + (\tfrac{1}{2\sqrt{3}}\cos\theta + \tfrac{1}{2}\sin\theta)\cos\theta\sigma - (-\tfrac{1}{2\sqrt{3}}\sin\theta + \tfrac{1}{2}\cos\theta)\sin\theta\nu\sigma)$$
$$R_{1y} = (\tfrac{1}{2} + (\tfrac{1}{2\sqrt{3}}\cos\theta + \tfrac{1}{2}\sin\theta)\sin\theta\sigma - (-\tfrac{1}{2\sqrt{3}}\sin\theta + \tfrac{1}{2}\cos\theta)\cos\theta\nu\sigma)$$
$$R_{2x} = (\tfrac{1}{2\sqrt{3}} + (\tfrac{1}{2\sqrt{3}}\cos\theta - \tfrac{1}{2}\sin\theta)\cos\theta\sigma - (-\tfrac{1}{2\sqrt{3}}\sin\theta - \tfrac{1}{2}\cos\theta)\sin\theta\nu\sigma)$$

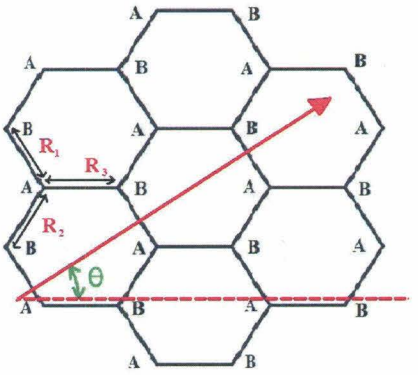

Figure 5: Strain along an arbitrary direction.

$$R_{2y} = (-\tfrac{1}{2} + (\tfrac{1}{2\sqrt{3}}\cos\theta - \tfrac{1}{2}\sin\theta)\sin\theta\sigma - (-\tfrac{1}{2\sqrt{3}}\sin\theta - \tfrac{1}{2}\cos\theta)\cos\theta\nu\sigma)$$

$$R_{3x} = -\tfrac{1}{\sqrt{3}}(1 + \cos\theta\cos\theta\sigma - \sin\theta\sin\theta\nu\sigma)$$

$$R_{3y} = -\tfrac{1}{\sqrt{3}}(\sin\theta\sin\theta\sigma - \cos\theta\cos\theta\nu\sigma)$$

To calculate the new $E_{2D} = \pm\sqrt{f(k)^* f(k)}$, $f(k) = \sum_k e^{i\vec{k}\cdot\vec{R}_k} t_k$, k = 1, 2, 3 must be recomputed. To evaluate the transfer integrals, the approximation that t_k scales as $\frac{1}{|R|^2}$ will be used. Values of the band gap as a function of strain and angle were numerically computing through iterating through values of θ from 0.0 to 1.0, and values of σ from 0.0 to 1.0. Figure 6 is plot of band gap as a function of strain and the angle of the strain:

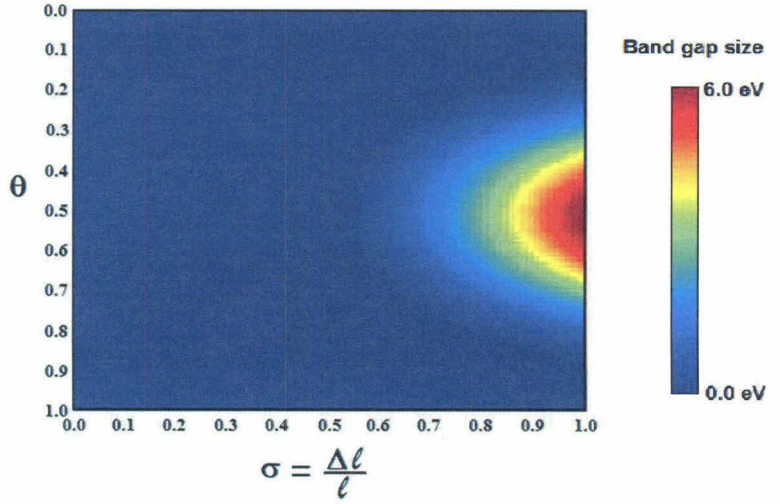

Figure 6: Plot of the band gap as a function of strain and the angle of strain. Note that a strain of greater than 50% is needed to induce a gap, a magnitude which would cause the graphene lattice to melt, and invalidate our three nearest neighbor approximation we used in our tight binding calculation.

As seen in Figure 6, graphene will continue to exhibit Dirac-like behavior until the strain is greater than 50%, a magnitude which would cause the graphene lattice to melt and invalidate the three nearest neighbor approximation used in the tight binding calculation.

3.2 Phonon-mediated inelastic tunneling

In this section we will look into phonon-mediated inelastic tunneling, as we will return to it later. Phonon-mediated inelastic tunneling is caused by out of plane phonons at the K and K′ points, which cause coupling between the nearly free electron bands at Γ and the Dirac fermions in the π bands near K and K′. [7]

Tunneling currents are determined by the local density of states near the tip, typically around 5 Åabove the sample.[8] For graphene, according to Terseoff and Harmann[21], we should have $\frac{dI}{dV} \approx {\Psi_\Gamma}^2 N_\Gamma(E) + {\Psi_K}^2 N_K(E)$, where N_Γ is the density of states of the nearly free electron bands and $N_K(E)$ is the density of states of the π bands. In the presence of phonon-mediated inelastic tunneling, we have $\frac{\Psi_\Gamma}{\Psi_K} \sim 10^4$.[7] Therefore, $N_\Gamma(E)$, the density of states of the nearly free electron band, will dominate the tunneling density of states.

We will discuss here the model developed by Wheling et al.[7] to explain how phonon-mediated tunneling affects scanning tunneling spectroscopy.[11] The Dirac fermions at K and K′ can be described by the Hamiltonian $H = \sum_{\nu=\pm,q} \nu E(k) c_q^\dagger c$, where $c_q^\dagger$ is the creation operator of an electron in the π band with a momentum q, and $\nu = \pm$ is an index for the conduction and valence bands. The nearly free electron bands at Γ have a minimum energy at $E_\sigma = 3.3$ eV, and can be approximated by a flat band $H = \sum_q d_q^\dagger E_\sigma d_q$, where $d_q^\dagger$ is the creation operator of an electron with momentum q.

The out of plane phonons at K and K′ can be described by $H_{ph} = \hbar\omega_a \sum_k a_k^\dagger a_k$, where $a_k^\dagger$ is the creation of a phonon of frequency ω_a. The phonons cause scattering between the nearly free electron bands and π bands. This interaction can be described by $V = \lambda \sum_{v,q,k} ({d_{k+q}}^\dagger c_{v,q} + c_{v,q}^\dagger d_{k+q})(a_k + {a_k}^\dagger)$.

The noninteracting electron Green's function is described by

$$G^0(q, i\omega_n) = \begin{bmatrix} \frac{1}{i\omega_n - E_\sigma} & 0 & 0 \\ 0 & \frac{1}{i\omega_n - E(q)} & 0 \\ 0 & 0 & \frac{1}{i\omega_n + E(q)} \end{bmatrix}$$

where ω_n are the fermionic Matsubara frequencies. The non-interacting phonon Green's function is described by $D^0(i\Omega_m) = \frac{2\omega_a}{\Omega_m^2 + \omega_a^2}$. Therefore, the aforementioned electron-phonon interaction can be rewritten in matrix notation as

$$M_- = \begin{bmatrix} 0 & \lambda & 0 \\ \lambda & 0 & 0 \\ 0 & 0 & 0 \end{bmatrix} \text{ and } M_+ = \begin{bmatrix} 0 & 0 & \lambda \\ 0 & 0 & 0 \\ \lambda & 0 & 0 \end{bmatrix}$$

so that the electronic self-energy can be expressed as

$$\sum(i\omega_n) = -\frac{1}{\beta} \sum_{v,\Omega_m} D^0(i\Omega_m) M_\nu G^0(r = 0, i\omega_n - i\Omega_m) M_\nu \qquad (1)$$

The self-energy is diagonal and for ω small compared to the Dirac energy bandwidth (~ 6 eV), the components are $\sum_{1,1}(\omega + i\delta) = \sum'_{1,1}(\omega + i\delta) + i\sum''_{1,1}(\omega + i\delta)$, where:

$$\sum'_{1,1}(\omega + i\delta) \propto (\omega - \omega_a) \log|\tfrac{\omega - \omega_a}{W}| + (\omega + \omega_a) \log|\tfrac{\omega + \omega_a}{W}|$$

$$\sum''_{1,1}(\omega + i\delta) \propto -\Theta(|\omega| - \omega_a)|\omega - \mathrm{sgn}(\omega)\omega_a|$$

Integrating the interacting Green's function $G^{-1} = G^{(0)-1} - \sum(\omega)$ over momentum space gives the total density of states, $N(\omega) = -\frac{1}{\pi}\mathrm{Tr}\mathrm{Im}G(r = 0, \omega + i\delta)$. As shown in Figure 6, the resulting total density of states are V-shaped and indistinguishable from that of the π bands. The only difference is a small shift of the Dirac point that occurs with increasing coupling strength.

At these low energies, the density of states in nearly free electron bands are described by $N_\Gamma(\omega) = -\frac{\sum''_{1,1}(\omega + i\delta)}{\pi|\omega - E_\sigma - \sum_{1,1}(\omega + i\delta)|^2}$. This density of states will vanish for energies less then E_σ if there is no electron-phonon interaction. With the phonon-electron interaction present, for electron energy $\omega > \omega_a$, where ω_a is the phonon frequency, the nearly free electron bands will mix with the π bands, resulting in a band gap of width $\pm\omega_a$. Outside

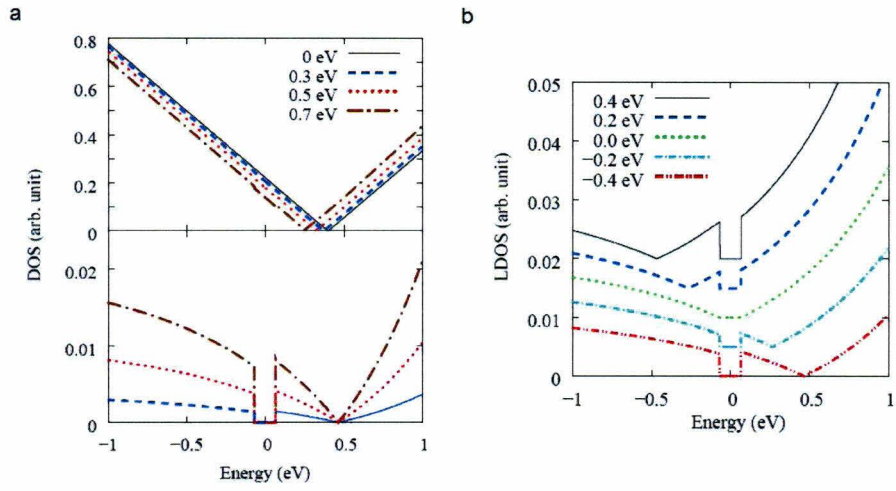

Figure 7: a. The density of states for coupling strengths $\lambda = 0, 0.3, 0.5, 0.7$ eV. The top pannel shows the total density of states while the lower panel shows the density of states of the nearly free electron band. b. The density of states of the nearly free electron band. Changing the chemical potential μ will causes the Dirac point to shift. (Images taken from Phonon-mediated tunneling into graphene. T.O Wehling, et. al 2008.)

of this bandgap, the density of states of the nearly free electron band will resume to the V-shaped behavior of the density of states of the π bands. Since the tunneling spectra will be dominated by the density of states of the nearly free electron band, Wehling et. al [7] predict a tunneling spectra for graphene as depicted in Figure 7. This was observed by Z. Yhang et al. from Berkeley in 2008 [5], as shown in Figure 3.

4 Results

4.1 Topography

We conducted our STM graphene measurements at 77.7 K and pressures below 10^{-6} torr. To calibrate the STM to high accuracy, topography scans were taken of a graphite sample (Figure 18). The image exhibits a triangular lattice structure which is due to Bernal stacking.

STM topography scans of graphene over a 2.2 nm by 5.0 nm region(Figure 8a) and 8.6 nm by 8.6 nm (Figure 8c) region are shown. The scans exhibit a hexagonal lattice structure, as well as significant corrugations. The height variations due to these corrugations are on the order of $\pm$ 0.5 nm, over the range of 10 nm.

In figure 8b is a histogram of the height variations over region of 8a. In order to compare the corrugations of the graphene sample with that of a $Si0_2$ substrate, AFM measurements were taken of a SiO_2 substrate over a 8.6 nm by 8.6 nm region. Figure 8d shows the histogram of the height variations of both the SiO_2 substrate and the graphene sample over the 8.6 by 8.6 nm region. The correlation between the histograms demonstrate that corrugations in the graphene are due to its partial conforming to underlying silicon dioxide substrate.

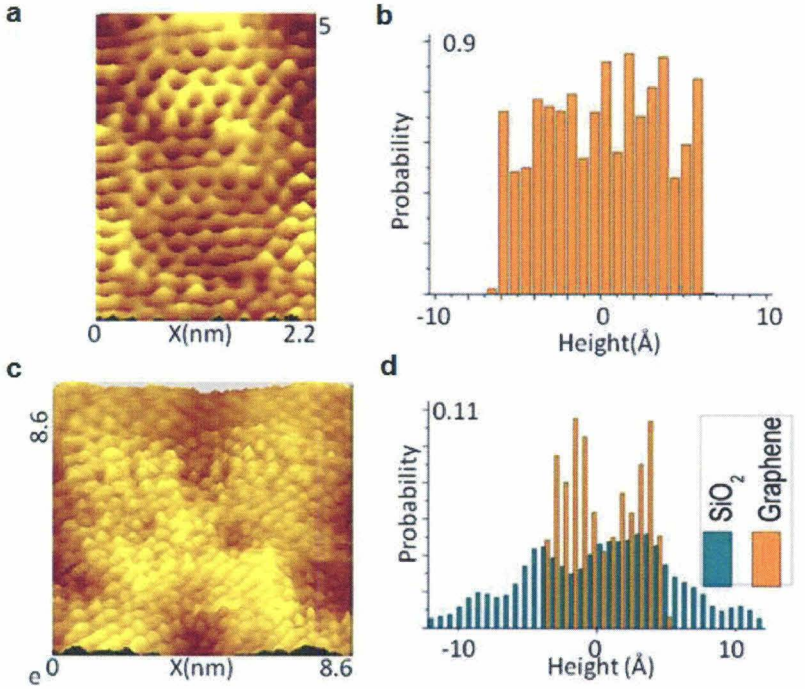

Figure 8: a. A STM scan of graphene over a 2.2 nm by 5.0 nm region. b. A histogram of the height variation over the region scanned in a). c. A STM scan of graphene over a 8.6 nm by 8.6 nm region. d. A histogram of the heigh variations of an $S0_2$ substrate and the height variations over the region in c). The two histograms show apparent correlation

4.2 Conductance Maps

Scanning tunneling spectroscopy measurements were performed over a 5.0 nm by 2.2 nm region. Conductance ($\frac{dI}{dV}$) maps at various bias voltages are shown in Figure 9 and a spatial map of the Dirac voltage is shown in Figure 10.

At low bias voltages, the conductance appears to correlate fairly well with the overall topography. As the bias voltage is increased, the overall conductance becomes more

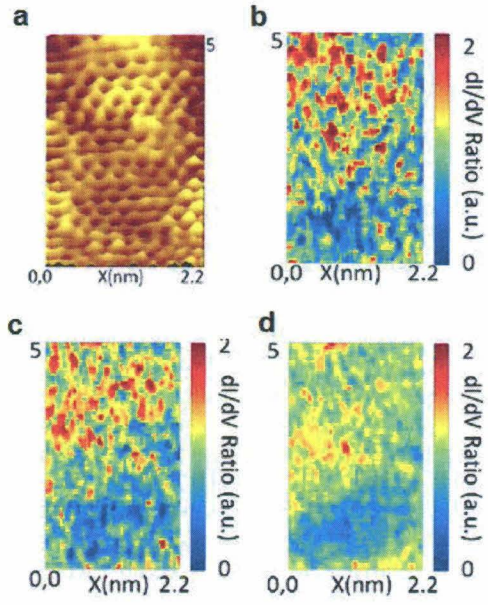

Figure 9: a. A topography scan over a 2.2 nm by 5.0 nm region. b-d. Conductance maps at bias voltages of 0 meV, 80 meV and 240 meV. As the bias voltage is increased, the overall correlation of the conductance with topography is reduced

homogenous, indicating that the conductance modulations are primarily associated with the low energy charge excitations which are influenced by changes in topography and a strained lattice.

Charge impurities in the SiO_2 substrate would cause a shift in the Dirac voltage and therefore could be a cause for the deviation from Dirac behavior found in the tunneling spectra. The spatial map of the Dirac voltage is fairly homogenous, while at low bias voltages, the spatial conductance maps follow the overall topography of the sample.

The lack of correlation between the Dirac voltage and conductance maps at low bias voltage (Figure 10) indicates that charge impurities likely are not the main cause for the variations in the local density of states of graphene.

4.3 Strain Maps

In Figure 11 is a fast Fourier transform of the topography scan from figure 4a. We observe a distorted hexagon (Figure 11), indicating significant distortion to the lattice structure of the graphene sample.

In order to quantify these lattice distortions, the displacement $u(x, y) = u_x\vec{x} + u_y\vec{y}$,

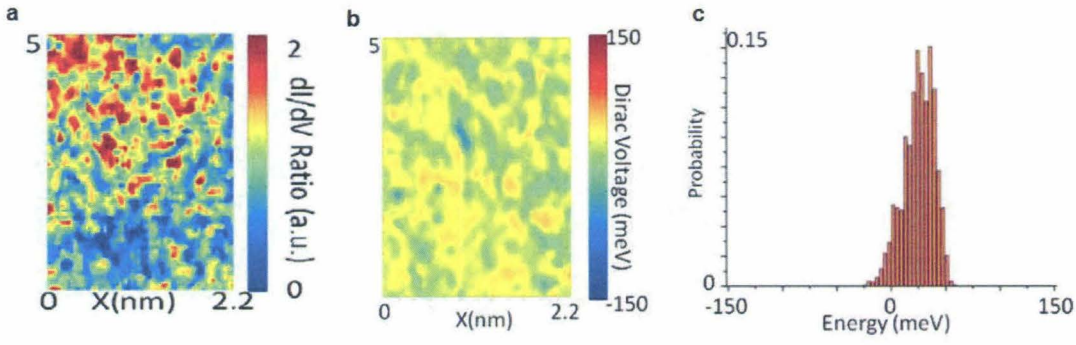

Figure 10: a. A spatial map of the conductance at a low bias voltage. b. A spatial map of the Dirac voltage. c. A histogram of the Dirac voltage over the spatial region in b. It is apparent from the histogram that the Dirac voltage is fairly homogenous in the spatial region in b. Overall, there is a lack of correlation between Dirac voltage and conductance at low bias voltage.

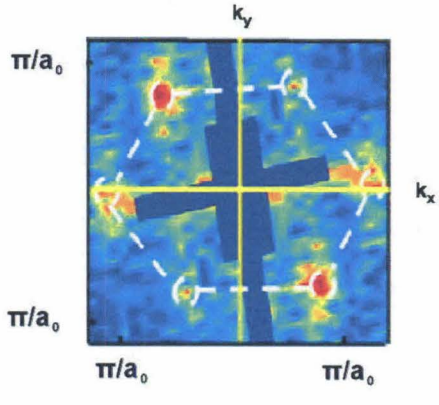

Figure 11: A fast Fourier transform of the earlier 5.0 nm by 2.2 nm topography scan. The distorted hexagon indicates significant distortion to the lattice structure of the graphene sample

where u is the deviation of the local lattice vector from the equilibrium lattice vector, was used to compute strain maps over the topography region in figure 8a(Figure 12). This displacement was computed by taking the Fourier transform of a group of atoms, computing the displacement of the local reciprocal lattice vectors, and inverse Fourier transforming that displacement back into real space.

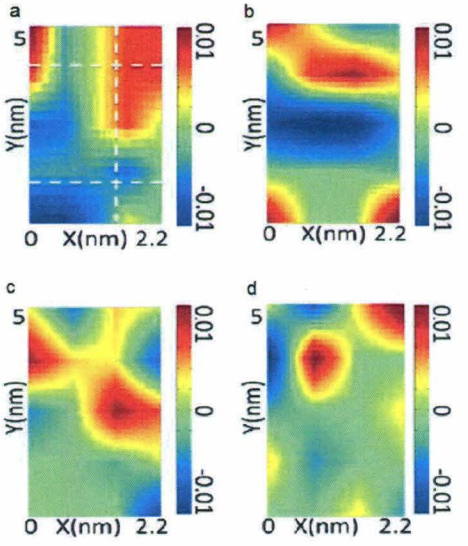

Figure 12: a. The scalar strain, $S_o = \frac{u(x,y)}{a_o}$. b. $S_{xx} = \frac{du_x}{dx}$ c. $S_{yy} = \frac{du_y}{dy}$ d. $S_{xy} = S_{yx} = \frac{\frac{du_x}{dy} + \frac{du_y}{dx}}{2}$.

Figure 12a is a map of the scalar strain, or $S_o = \frac{u(x,y)}{a_o}$, while Figures 12b-d show the strain tensor components, $S_{xx} = \frac{du_x}{dx}$, $S_{yy} = \frac{du_y}{dy}$ and $S_{xy} = S_{yx} = \frac{\frac{du_x}{dy} + \frac{du_y}{dx}}{2}$ respectively. Overall, we can see that the scalar strain appears roughly follow the topography.

To investigate the correlation between low charge excitations and strain, a correlation number between a conductance map at low bias voltage (Figure 9) and the scalar strain (Figure 12a) was computed as follows:

$$C = \frac{\int (f(\vec{r}) - \bar{f})(g(\vec{r} + \vec{R}) - \bar{g}) d^2 r}{\sqrt{A_{f,f}(0) A_{g,g}(0)}} \qquad (1)$$

where

$$A_{f,f}(\vec{R}) = \int f(\vec{r}) - \bar{f})(f(\vec{r} + \vec{R}) - \bar{f}) d^2 r$$

and f and g are the low bias voltage conductance map and scalar strain map.

A value of -1 implies complete anticorrelation, +1 indicates complete correlation and 0 indicates no correlation at all. The correlation number for the scalar strain and low bias voltage conductance map (40 meV) was 0.44. However, at highier bias voltage conductance maps (240 meV), the correlation went down to 0.12, indicating that strain has a much more pronounced affect on the low charge exitations of graphene.

4.4 Phonon-mediated inelastic tunneling

As discussed earlier, due to phonon-mediated inelastic tunneling, the tunneling density of states are dominated by the density of states of the nearly free electron bands $N_\Gamma(E)$.[7] Therefore, to see the correlation between strain and the deviation in the tunneling spectra, N_Γ was fitted to the observed tunneling spectra, where:

$$N_\Gamma(\omega) = -\frac{\sum''_{1,1}(\omega+i\delta)}{\pi|\omega-E_\sigma-\sum_{1,1}(\omega+i\delta)|^2} \qquad (1)$$

with $E_\sigma = 3.3eV$ and the electron self-energy

$\sum_{1,1}(\omega+i\delta) = \sum'_{1,1}(\omega+i\delta) + i\sum''_{1,1}(\omega+i\delta)$, with:

$$\sum'_{1,1}(\omega+i\delta) \propto (\omega-\omega_a)\log|\tfrac{\omega-\omega_a}{W}| + (\omega+\omega_a)\log|\tfrac{\omega+\omega_a}{W}|$$

$$\sum''_{1,1}(\omega+i\delta) \propto -\Theta(|\omega|-\omega_a)|\omega-\mathrm{sgn}(\omega)\omega_a|$$

The phonon frequency, ω_a is used as a fitting parameter.

In Figure 13a is a line cut of tunneling spectra, along the direction depicted in 13g. The spectra along this line cut are primarily U-shaped, and from the strain map in 13g, correspond to a region of substantial strain. The theoretical fit to an observed tunneling spectra (Figure 13c) along this line cut agrees fairly well and corresponds to an out-of-plane phonon frequency $\hbar\omega_a$ of 44 meV. In Figure 13b is a line cut with tunneling spectra exhibiting more V-shaped behavior. This line cut corresponds to a region of relaxed strain. The theoretical fit from a tunneling spectra (Figure 13e) in this region corresponds to a lower phonon frequency of $\hbar\omega_a$ of 26 meV. Therefore, this apparent correlation between the observed tunneling spectra and strain maps seems to indicate that strain-induced modulations in conductance and phonon-mediated inelastic tunneling

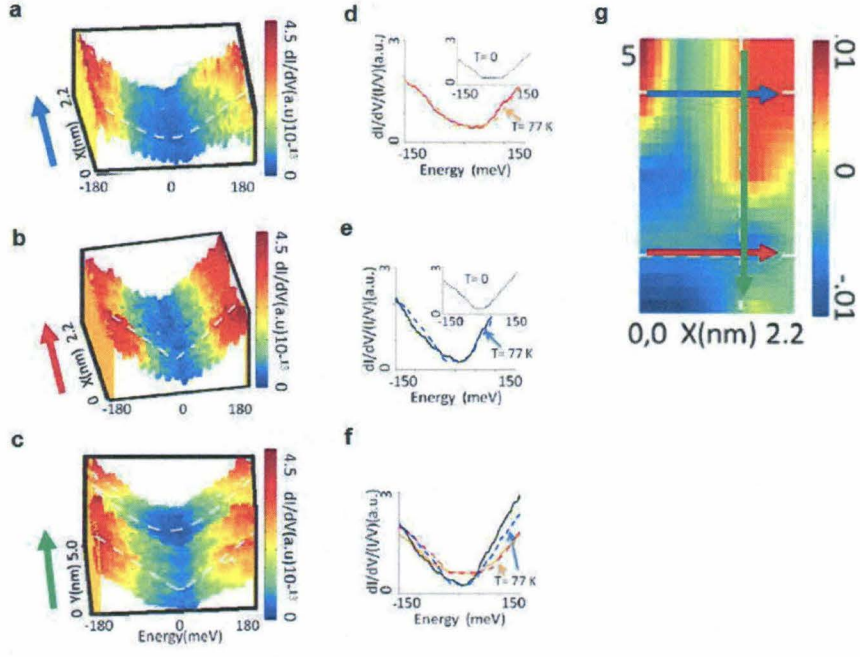

Figure 13: **a - c)**. Line cuts of tunneling spectra along the directions indicated by g. **a**. A line cut with tunneling spectra that is primarily U shaped. **b**. A line cut with tunneling spectra which is primarily v-shaped. **c**. A line cut where the tunneling spectra goes from being primarily v-shaped to primarily u-shaped. **d**. A theoretical curve fit of a primarily u-shaped tunneling spectra from **a)** with a phonon frequency of $\hbar\omega_a = 44meV$. **e**. A theoretical curve fit of a primarily v-shaped tunneling spectra from **b)** with a phonon frequency of $\hbar\omega = 26meV$. **f**. A comparison of the fits from **d)** and **e)** **g**. The region from which the line cuts of tunneling spectra were taken from. The directions of the line cuts are indicated by the arrows in the figure.

are one of the primary reasons for the deviation of tunneling spectra in graphene from Dirac-like behavior.

5 Current/Future Projects

5.1 STM on gated graphene

While phonon-mediated inelastic tunneling contributes to the deviation in the spectra from Dirac behavior, it is likely not the only cause. Given that the phonon-mediated tunneling is due to low energy exitations, we hope that by gating our graphene sample to change the the Fermi level, we may be able to gain insight into other causes for the deviation from Dirac behavior.

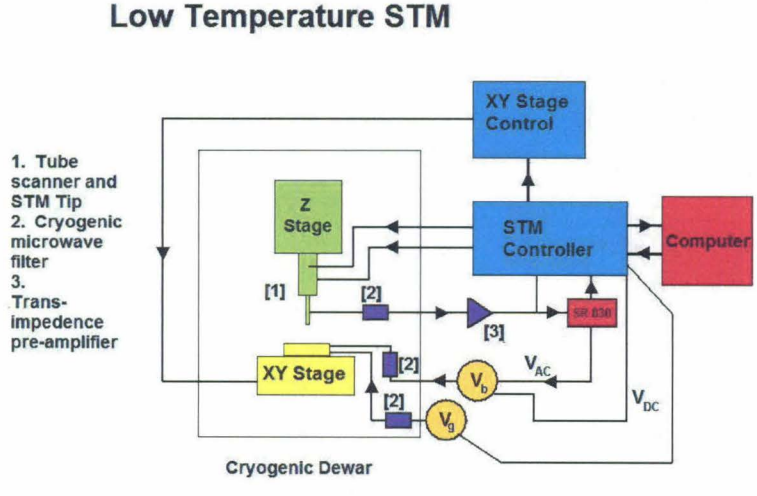

Figure 14: A block diagram of the STM setup with gate voltage

We currently have a gated graphene sample loaded within the STM and are attempting to conduct measurements.

5.2 Future projects: STM on graphene atomic switches

We are interested in the physics behind graphene switching devices discovered by Professor Marc Bockrath's research group. [22] A large current is applied accross a graphene sheet breaking the bonds between carbon atoms, forming a nano-scale gap. When the applied bias voltage is below 2 volts, the current remains negligably low. As the bias voltage is increased to the 2.5-4 volt range, the current increases dramatically, up to a maximum of 0.65 mA at around 5 V. Applying bias voltages of over 6 volts results in a negligable current once again. Thus, by applying different voltages corresponding to ON and OFF states, a graphene switching device can be constucted. Such a switching device has uses in logic gates and information processing applications. It is believed that the switching in the graphene occurs due to the formation of linear chains of carbon atoms. The formation and breakdown of the linear carbon chain depends on the applied bias voltage. These switching devices will also provide us with an opportunity to look at the edge states of graphene, and whether the edge states which form are armchair states or zizzag states.

6 Conclusion

In summary, we obtained atomically resolved scanning tunneling microscopy and spectroscopy of graphene. The topography scans exhibited corrugations in the graphene sample, which are due to its partial conforming to the underlying silicon dioxide substrate. More importantly, the observed tunneling spectra exhibited deviations from the expected Dirac behavior. Charge impurities are unlikely the main cause for this, as there was little correlation spatially between the Dirac voltage and low bias conductance maps. Instead, substrate induced strain in the graphene sample and phonon-mediated inelastic tunneling are likely the main cause for the deviation from Dirac behavior observed in the tunneling spectra. Because this phenomenon occurs with low energy exitations, gating the graphene sample will prove to be informative, and hopefully shed light into other causes for deviation from Dirac behavior.

7 Experimental Setup

7.1 Scanning Tunneling Microscopy

The primary experimental tool used in these studies is the scanning tunneling microscope (STM). The STM is an excellent experimental tool to study graphene due to its atomic scale resolution. STM operates on the principle of quantum tunneling, where the conducting tip of the microscope is brought to within subnanometer distance of a sample and an applied bias voltage causes electrons to tunnel through the vacuum in between the tip and the sample.

The resulting tunneling current can provide extensive information about the sample surface.[19,20] Using the Fermi's golden rule, there is a transmission rate of electrons from the energy states of the sample to the energy states of the tip:

$W = \frac{2\pi}{\hbar} M_{ts}^2 \delta(E_{tip} - E_{sample}) \Rightarrow$

$I = \frac{4\pi}{\hbar} \int_{-\infty}^{\infty} (f(E_F - eV_b - E) + f(E_F + E)) \rho_{sample}(E_F - eV_b + E) \rho_{tip}(E_F - E) M_{st}^2 dE$ (1)

where f is the Fermi-Dirac distribution, ρ represents the density of states and $\hbar$ is Plancks constant. The barrier between the tip and the sample will be treated as a 1D rectangular potential barrier with a width of d. Using time dependent pertubation theory, the wavefuctions for the exact Hamiltonian will be approximated as [5]:

$\Psi_s(z) = ae^{-\chi z}$ for z ≥ 0

$\Psi_t(z) = be^{\chi z}$ for z $\leq d$

where $\chi = \sqrt{\frac{2m(V_o - E)}{\hbar^2}}$. Thus, $\Psi_s(z)$ is a correct solution for $z \leq d$ and $\Psi_t(z)$ is a correct solution for $z \geq 0$. Thus, inserting the general solution $\Psi(t) = c(t)\Psi_s e^{\frac{-E_s t}{\hbar}} + d(t)\Psi_t e^{\frac{-E_t t}{\hbar}}$ into the time dependent Schrodinger equation:

$H\Psi(t) = i\hbar \frac{d\Psi(t)}{dt}$ where $H = H_o + H_T$

which gives $M_{ts} =< \Psi_t | H_T | \Psi_s > \propto \exp(-2\chi d). \Rightarrow$

$I \propto \exp(-2\chi d).$

Therefore, the resulting current is proportional exponentially to the distance between the STM tip and the sample, and can provide information about the topography of the sample.

Now, consider (1), at low temperatures and with a constant tunneling matrix:

$I \propto \frac{4\pi}{\hbar} \int_0^{eV_b} \rho_{sample}(E_F - eV_b - E)\rho_{tip}(E_F + E)dE$

Assuming that the tip density of states is constant, and taking the derivative with respect to V_b:

$\frac{dI}{dV_b} \propto \rho_{sample}(E_F - eV_b)$

so that $\frac{dI}{dV_b}$ is proportional to the local density of states of the sample.[1] Therefore, the tunneling current can provide information about both the topography and its derivative with respect to bias voltage information about the local density of states of the sample. Due to graphene's 2D nature and its conical band structure, its density of states would be linear as a function of energy, vashishing at the Dirac point implying a V-shaped tunneling spectra.

7.2 STM specifics

The measurements on graphene were conducted on a homebuilt, cryogenic STM capable of temperature measurements from room temperature down to 6.2K. The STM is also capable of magnetic fields up to 7 Tesla and achieving base pressures below 10^{-10} torr at 6 K.

7.2.1 Tube Scanner and Coarse Movement Stages

The control and movement of the STM comes from the cylindrical tubescanner and the coarse movement stages. The tubescanner consist of piezo-electric crystal and provides

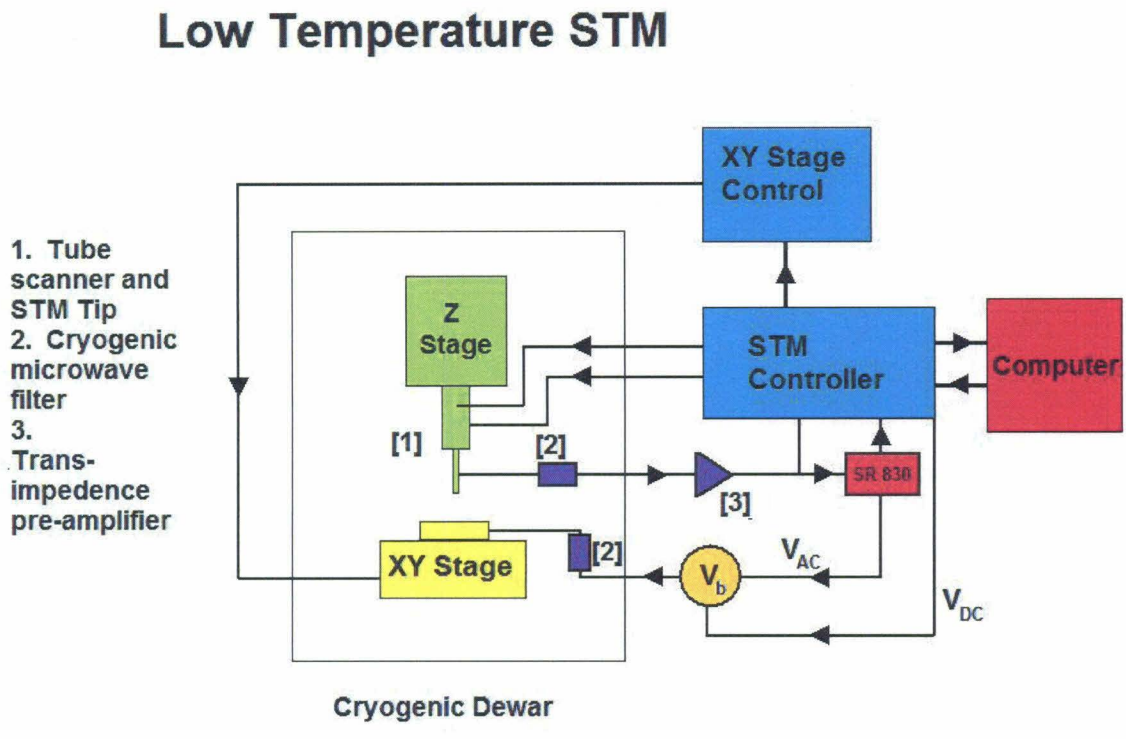

Figure 15: A block diagram of the STM setup

fine control movement. Therefore, by applying voltages in the range from 10-100 volts accross the four quadrants of the tube scanner, the tubescanner can go from fully retracted to fully extended, providing a movement range 2 microns in the z direction. The tube scanner can also achieve lateral movement in both the x and y directions with a range of 10 microns. The spatial scans conducted by the STM are done through this lateral movement of the tubescanner.

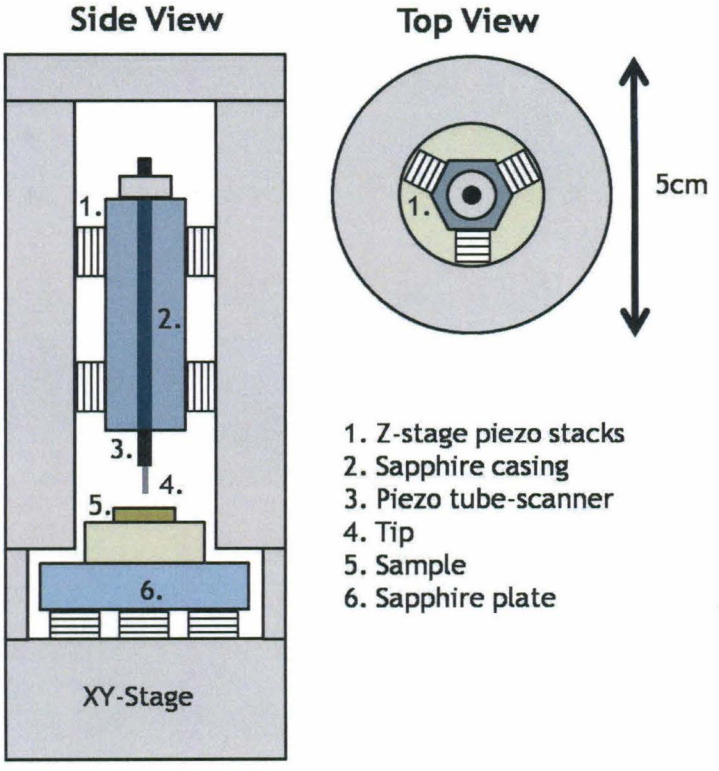

Figure 16: A diagram of the STM head

While the tubescanner provides fine control movement of the position of the tip relative to the sample, coarse movement stages provide a much larger range of movement. The coarse z-stage moves the tubescanner 1 micron per step. This, combined with the piezo-electric control of the tubescanner provides a safe method of bringing the tip within tunneling range of the sample. First, the voltage applied to the tubescanner is gradually increased. If no tunneling current is detected as the tube scanner becomes fully extended, the tube scanner is retracted, and the coarse z-stage moves a step closer to the sample. The process is therefore repeated until a tunneling current is detected.

The course XY stage provides a range of lateral movement of 1 mm, with 100 nm movement per step. The XY stage allows for the study of fairly imhomogenous samples. Additionally, it allows for the correction of the tip position, in case the tip is positioned over a conducting part of the surface but not over the part of the surface desired for study.

7.2.2 Cryogenics

The STM is capable of maintaining a temperature of 6.2 K near the sample. This is achieved by placing the STM body inside a cryogenic dewar, and filling the dewar with either liquid nitrogen (77 K) or liquid Helium (4.2 K). The STM head is constructed from materials with low coefficients of thermal expansion so that the STM can operate in a large range of temperatures.

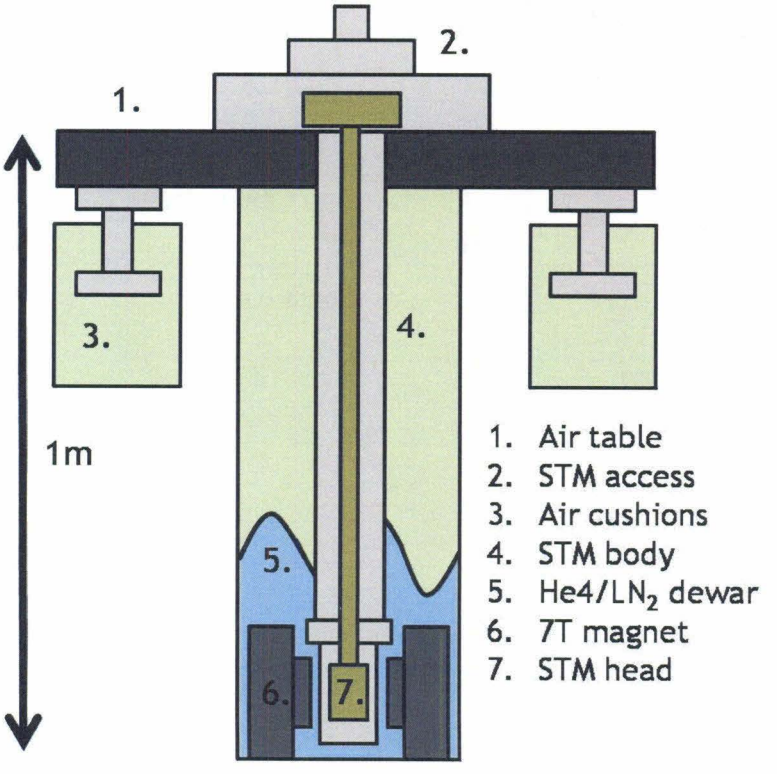

Figure 17: STM diagram

7.2.3 Modes of Operation

The STM can conduct both topographic and spectroscopic scans. Topography scans are performed by moving the tip laterally over the sample over a specified range. This movement is achieved through the tubescanner. As the tip is moved over the sample, a constant tunneling current through a feedback system, which moves the tip away from the sample if the tunneling current is too high and closer to the sample if the tunneling current is too low. Because the tunneling current is exponentially proportional to the distance between the tip and the sample, a very precise measurement of sample topography can be through this method. The STM is often used for resolving individual atoms, as atomic resolution was achieved in our scans of graphene.

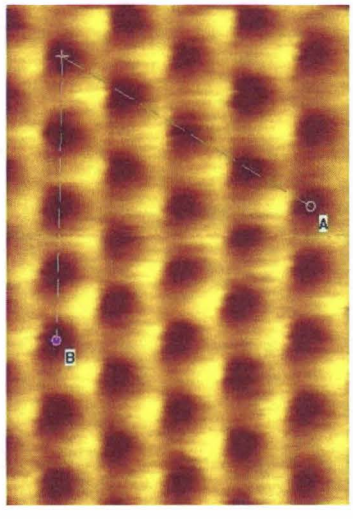

Figure 18: A topography scan of graphite with atomic resolution. The scan was performed while calibrating the STM for high accuracy. The image exhibits a triangular lattice structure which is due to Bernal stacking.

The STM can also be used for spectroscopy and conductance maps. In scanning tunneling spectroscopy, the tip remains at its position over the sample and the bias voltage is varied over a range of values. As a result, the tunneling current as a function of bias voltage can be measured, and $\frac{dI}{dV}$, the tunneling conductance, can provide information about the local density of states (LDOS) of the sample. By combining the topography mode and spectroscopy mode, spatial conductance maps can be taken with the STM. This is achieved by taking individual spectra at various locations of the sample and therefore providing spatial resolution of the local density of states of the sample.

7.3 STM tip fabrication

Tips for the scanning tunneling microscope (STM) are fabricated from platinum-iridium wire, mainly because platinum-iridium is unreactive with air and the process for fabricating tips from platinum-iridium is relatively simple. The fabrication process of platinum-iridium tips involves first the mechanical shearing of platinum-iridium wires followed by the electrochemical polishing of the resulting tips. Mechanical shearing is accomplished using wire cutters to shear tips from a platinum-iridium wire. Only optically sharp tips are kept, as optical sharpness is required so that the tip can be positioned exactly above the micron sized graphene sample.

The electrochemical etching process involves placing the tips in a solution of calcium chloride dihydrate and an AC voltage of 5 V is applied between the solution and the tip for a few seconds. This sharpens the tip atomically, improving the quality of tunneling, as well as leaving a broad tip surface. The broad surface tip surface allows the tip density of states to be linear, so that the tunneling conductance remains a good approximation of the local density of states of the sample.

7.4 Frabrication of graphene sample

The graphene sample under investigation in this project was prepared by Professor Chun Ning Lau's group from the University of California at Riverside and was fabricated through the process of mechanical exfoliation.[1]. The sample is several microns in size and is located on top of a silicon dioxide substrate containing gold contact pads approximately 160 microns away from the graphene sheet. Gold wires connect the pads to the graphene sample. These gold pads and wires were etched onto the substrate through photolithography processes. In order to remove possible residual photoresist resulting from the photolithography process, the graphene sample was annealed at a temperature of 400 C° for 15 minutes in an oxygen environment using a Hevi-Duty high temperature oven with an Omega CN2011 temperature controller.

7.5 Positioning STM tip over the sample

Due to the size of the graphene sample, which is barely resolvable to the naked eye, one of the most difficult tasks was positioning the STM tip over the graphene sample. In order to provide the needed magnification, an optical microscope was configured and used in this task. Even with this magnification, moving the sample on the XY stage right underneath the sample with complete accuracy is not achievable. In the scenario where the STM is operating and the tip is positioned over the surrounding gold, the XY stage must be used to reposition the tip over the graphene sample. This is a rather cumbersome task, as the STM has a maximum range of around 1 square micron in scanning. Therefore, our field of view while running the STM is at most 1 micron, while our precision using the optical microscope is limited to 10 microns.

7.6 Acknowledgements

Overall, I would like to extend thanks to Professor Nai-Cheng Yeh, Marcus Teague and Andrew Beyer. I would also like to thank the NSF for funding this project.

8 References

1. Geim, AK. 'The rise of graphene'. Nature materials, 6(3), 183-191. (2007)
2. Novoselov, K.S. 'Two-dimensional gas of massless Dirac fermions in graphene'. Nature 438, 197-200 (2005)
3. Andrei, E. 'Scanning Tunneling Spectroscopy of graphene a glimpse into the world of a relativistic particle' arXiv:0803.4016 Nature (2008) (under review)
4. Ishigami, M. 'Atomic Structure of Graphene in SiO_2'. Nanoletters. 7(6), 1643-1648 (2007)
5. Zhang, Y. 'Giant phonon-induced conductance in scanning tunnelling spectroscopy of gate-tunable graphene'. Nature physics 4.8, 627-630. (2008)
6. Parga, A.L. 'Periodically rippled graphene: growth and spatially resolved electronic structure'. Physical Review Letters. (2008)
7. Wehling, T. O. 'Phonon mediated tunneling into graphene. Phys. Rev. Lett. 101 216803 (2008).
8. Rutter, G. M. et al. Scattering and interference in epitaxial graphene. Science 317, 219-22 (2009)
9. Landau, L.D. Lifshitz, E.M. *Statistical Physics, Part I* (Pergamon, Oxford, 1980.)
10. Novoselov, KS. 'Two-dimensional atomic crystals'. Proceedings of the National Academy of Sciences of the United States of America 102.30 :10451-10453. (2005)

11. Du, X. Approaching ballistic Transport in suspended graphene. Nature Nanotechnology 3, 491-495 (2008).
12. Bolotin, K. I. Ultrahigh electron mobility in suspended graphene. Solid State Commun. 146, 351-355 (2008).
13. Miao F. et al. Phase-Coherent Transport in Graphene Quantum Billards. Science 317, 1530-1533 (2007)
14. Martin, J. Observation of electron-hole puddles in graphene using a scanning single electron transistor. Nature Physics 4, 114-148 (2008)
15. Obraztsov, A. N. Chemical Vapour deposition: Making graphene on a large scale. Nature Nanotechnology 4, 212-213 (2009)
16. Heo, Jinseong. Probing electronic properties of carbon nanotubes. Ph.D thesis. California Institute of Technology. (2008)
17. Saito, R., Dresselhaus, G. Dresselhaus, M.S. *Physical Properties of Carbon Nanotubes.* (Imperial College Press, 1998).
18. Zhang, Y. Experimental observation of the quantum Hall effect and Berry's phase in graphene. Nature 438, 201-204 (2005).
19. Wiesendanger, R. (1994) Scanning Probe Microscopy and Spectroscopy: Methods and Applications (Cambridge Univ. Press, Cambridge, U.K.).
20. C. Julian Chen, Introduction to Scanning Tunneling Microscopy, Oxford University Press New York (1993)
21. Tersoff, J., Hamann, D. R. Theory of the scanning tunneling microscope, Physical Review B 31, p. 805 - 813 (1985)
22. Standley, B. 'Graphene-based atomic-scale switches'. Nanoletters (2008)
23. Private communications/consultation with Professor Nai-Chang Yeh and Marcus Teague.